



Modeling planar hydraulic fractures driven by laminar-to-turbulent fluid flow



E.V. Dontsov^{a,*}, A.P. Peirce^b

^a Department of Civil and Environmental Engineering, University of Houston, Houston, TX, 77204, USA

^b Department of Mathematics, University of British Columbia, Vancouver, BC, V6T 1Z2, Canada

ARTICLE INFO

Article history:

Received 31 March 2017

Revised 3 August 2017

Available online 24 August 2017

Keywords:

Hydraulic fracturing

Turbulent flow

Level set

ABSTRACT

The goal of this study is to investigate the effect of turbulent fluid flow on the propagation of planar hydraulic fractures. Modeling a hydraulic fracture includes solving the elasticity equation that ensures the equilibrium of the rock, the fluid volume balance equation, and the fluid flow equation, which are solved together with a propagation condition. In this paper, the influence of turbulent flow is condensed into a single friction factor that influences the fluid flow equation, i.e. the relationship between the fluid flux and the pressure gradient. To capture all possibilities, an approximation for the friction factor, that captures the laminar, the turbulent, and the transitional flows is utilized in this study. Results for the axisymmetric fracture geometry demonstrate that the solution is dominated by turbulent flow at early times and near the source, while transitions to the laminar regime at larger times and close to the fracture tip. In the situation when turbulence dominates, the fracture is shorter and wider, since there is a strong pressure drop in the vicinity of the source, which causes the local fracture width increase. Results for a planar fracture propagating in a three stress layer geometry demonstrate that the turbulence leads to a more circular fracture that promotes height growth through a high stress zone.

© 2017 Elsevier Ltd. All rights reserved.

1. Introduction

Hydraulic fracturing is a technique used to create tensile cracks by injecting a pressurized fluid into a rock formation, which is primarily applied in petroleum industry to stimulate oil and gas wells (Economides and Nolte, 2000). High viscosity fluids have been used for many years for hydraulic fracturing. With the development of unconventional resources, in which the rock formations typically have much smaller pores, there is a tendency to use low viscosity fluids, such as a slick water that primarily consists of water with only a few additives. This transition to slick water results in a drop in the typical fluid viscosity value by nearly three orders of magnitude. As a result, the typical Reynolds numbers that are associated with the fluid flow are substantially increased and can be sufficient for the development of turbulent fluid flow within the fracture. The conventional models for hydraulic fracturing were developed for the high viscosity fluids and therefore the majority of the models consider exclusively laminar flow, see e.g. review papers (Adachi et al., 2007; Weng, 2015). In contrast, this study aims to account for the possibility of developing the turbulent fluid flow

and to investigate its effect on the propagation of planar hydraulic fractures.

The effects associated with turbulent fluid flow within hydraulic fractures have been considered previously. Early work includes (Nilson, 1981; Nilson and Morrison, 1986) that focused on the analysis of gas-driven hydraulic fractures in plane strain and Perkins-Kern-Nordgren (PKN) fracture geometries (Perkins and Kern, 1961; Nordgren, 1972). In addition, turbulent fluid flow is known to play a significant role in the modeling of hydraulically-driven cracks in glaciers (Tsai and Rice, 2010). More recent studies address the problem with respect to slick water hydraulic fracturing of unconventional reservoirs. For instance, the problem of a PKN fracture without leak-off is considered in Anthonyrajah et al. (2013), the analysis and scaling-based estimates for the fracture parameters associated with turbulence are presented in Ames and Bungler (2015), an analytical approximate solution for a PKN fracture with large leak-off is developed in Kano et al. (2015), while a similar solution for the PKN problem without leak-off is published in Zolfaghari et al. (2017b). An approximate analytical solution for a plane strain hydraulic fracture driven by a turbulent flow is derived in Zolfaghari et al. (2017a). As can be clearly seen from this paragraph, many studies have focused on simple fracture geometries, such as the PKN geometry, due to the possibility of obtaining analytical results and the ease

* Corresponding author.

E-mail addresses: edontsov@central.uh.edu, egordontsov@gmail.com (E.V. Dontsov).

of numerical implementation. In addition, the studies (Tsai and Rice, 2010; Ames and Bungler, 2015; Kano et al., 2015; Zolfaghari et al., 2017b) utilize the Gauckler-Manning-Strickler (Manning, 1891; Strickler, 1981) friction factor that applies for a fully turbulent fluid flow in a rough channel. Therefore, they focus on the limit, in which the fully developed turbulent flow is present within the whole fracture. This is not always the case, since the Reynolds number is proportional to the fracture width and becomes smaller in the vicinity of the fracture tip. As a result, there is always a region near the crack tip, within which the fluid flow is laminar. In order to capture the transition from laminar to turbulent fluid flow within the fracture, it is necessary to consider a friction factor that is able to capture the laminar fluid flow, the fully developed turbulent flow in smooth and rough fractures, and the transitional region. One such approximation for the friction factor was developed by Churchill in Churchill (1977). It was used recently in Dontsov (2016b) to analyze the influence of the laminar-to-turbulent transition of the fluid flow on the tip region of a hydraulic fracture and to estimate the distance at which the fracture width solution starts to deviate from the laminar solution due to the effect of turbulence. In addition, a numerical solution that captures the laminar-to-turbulent transition of a plane strain hydraulic fracture without leak-off is presented in Zolfaghari et al. (2017a). Similar to Dontsov (2016b), the latter numerical solution also utilizes Churchill's friction factor (Churchill, 1977) to capture the laminar-to-turbulent fluid flow inside the fracture.

The aim of this paper is two-fold. Firstly, it analyzes the transition from the laminar to fully turbulent solution for a radial or axisymmetric hydraulic fracture. Secondly, it employs the Implicit Level Set Algorithm (ILSA) (Peirce and Detournay, 2008; Peirce, 2015; Dontsov and Peirce, 2017) for a planar hydraulic fracture to study the effect of turbulent fluid flow on hydraulic fracture propagation. The ILSA scheme utilizes the approximate solution for the tip region problem (Dontsov and Peirce, 2015b) to advance the fracture's moving front, in which case accurate results can be obtained even on a coarse mesh. Churchill's friction factor (Churchill, 1977) is used for calculations due to its ability to capture the laminar, the turbulent, and the transitional regimes of the fluid flow. Note that the tip solution (Dontsov and Peirce, 2015b) that is used in the numerical algorithm assumes laminar flow. Therefore, the mesh is always kept sufficiently fine that the tip element is always within the laminar zone. The paper is organized as follows. Section 2 presents the governing equations for the problem. Section 3 analyzes the laminar-to-turbulent transition for the radial hydraulic fracture geometry. Finally, Section 4 presents the numerical results obtained using ILSA for a planar hydraulic fracture that propagates in an elastic medium with jumps in the confining stress field and summarizes the influence of turbulence on the solution.

2. Mathematical model

We consider the problem of a planar hydraulic fracture that propagates in a brittle permeable homogeneous elastic material, which is subject to a layered compressive stress field. Fig. 1(a) shows a schematic of the planar fracture footprint in the (x, y) plane, while Fig. 1(b) shows a schematic of the cross-section of the fracture along the x axis ((x, z) plane). The fracturing fluid is assumed to be Newtonian and the characteristic Reynolds numbers associated with the fluid flow are assumed to be sufficiently large that there is a possibility of having turbulent fluid flow inside the fracture. Note that the Reynolds number reduces gradually as the fracture becomes more narrow near the fracture front, in which case the flow transitions from (potentially) turbulent near the wellbore to laminar in the vicinity of the fracture tip, as shown in Fig. 1.

Before proceeding with the governing equations for the problem, it is convenient to introduce the following four scaled material parameters that affect the fracture evolution

$$\mu' = 12\mu, \quad E' = \frac{E}{1-\nu^2}, \quad K' = 4\left(\frac{2}{\pi}\right)^{1/2} K_{Ic}, \quad C' = 2C_L. \quad (1)$$

Here E is the Young's modulus, ν is the Poisson's ratio, and μ is the fluid viscosity, while K_{Ic} and C_L are the mode I fracture toughness and Carter's leak-off coefficient, respectively. The parameters E' , K' , and C' are assumed to be constant throughout the medium.

The elasticity equation that relates the fracture aperture w to the fluid pressure p along the crack and that ensures the elastic equilibrium of the material can be condensed into a single hyper-singular integral equation (Crouch and Starfield, 1983; Hills et al., 1996)

$$p(x, y, t) = \sigma^h(y) - \frac{E'}{8\pi} \int_{\mathcal{A}(t)} \frac{w(x', y', t) dx' dy'}{[(x' - x)^2 + (y' - y)^2]^{3/2}}, \quad (2)$$

where $\mathcal{A}(t)$ denotes area enclosed by the crack front $\mathcal{C}(t)$ (see Fig. 1) and $\sigma^h(y)$ is the prescribed *in-situ* geological stress field. For the three layer system considered in this paper $\sigma^h(y)$ can be written as

$$\sigma^h(y) = \sigma_2^h + (\sigma_3^h - \sigma_2^h) \mathcal{H}\left(y - \frac{1}{2}H\right) + (\sigma_1^h - \sigma_2^h) \mathcal{H}\left(-y - \frac{1}{2}H\right),$$

where \mathcal{H} denotes the Heaviside step function and σ_i^h ($i=1, 2, 3$) are the values of the compressive stresses in the three layers, as shown in Fig. 1.

The balance of fluid volume inside the fracture reads

$$\frac{\partial w}{\partial t} + \nabla \cdot \mathbf{q} + \frac{C'}{\sqrt{t-t_0(x, y)}} = Q_0 \delta(x, y), \quad (3)$$

where Q_0 is the injection rate, and the term involving C' captures fluid leak-off according to Carter's model, in which $t_0(x, y)$ signifies the time instant at which the fracture front was located at the point (x, y) . Note that $\mathbf{q} = (q_x, q_y)$ and $\nabla = (\partial/\partial x, \partial/\partial y)$ are respectively the flux and the gradient operator that act within the fracture plane.

To incorporate turbulent fluid flow into a hydraulic fracture model, it is necessary to consider the phenomenological Darcy-Weisbach equation, which relates the pressure drop along the flow to the fluid velocity according to

$$-\nabla p = f_D(Re, r) \frac{\rho}{2} \frac{U^2}{D} \frac{\mathbf{U}}{U}, \quad Re = \frac{\rho U D}{\mu}, \quad r = \frac{\epsilon}{D}, \quad (4)$$

where ρ is the mass density of the fluid, \mathbf{U} is the average fluid velocity vector and U is its magnitude, D is the hydraulic diameter of the channel, and f_D is the dimensionless friction factor. The latter friction factor depends on the Reynolds number Re and the relative roughness r , which is related to the absolute surface roughness ϵ . Experimentally obtained values of f_D are typically summarized on the so-called Moody chart (Moody, 1944), which plots the values for $f_D(Re, r)$ versus Re for different roughnesses r . An empirical approximation for f_D that is able to capture both laminar ($Re \lesssim 2300$), turbulent ($Re \gtrsim 4000$), and transitional ($2300 \lesssim Re \lesssim 4000$) regimes was proposed in Churchill (1977). The latter approximation was obtained originally for circular pipes and adjusted in Dontsov (2016b) for hydraulic fractures. The adjusted expression for the friction factor can be written as

$$f_D = 8 \left(\left(\frac{12}{Re} \right)^{12} + (A + B)^{-1.5} \right)^{1/12}, \quad (5)$$

where the parameters A and B are given by

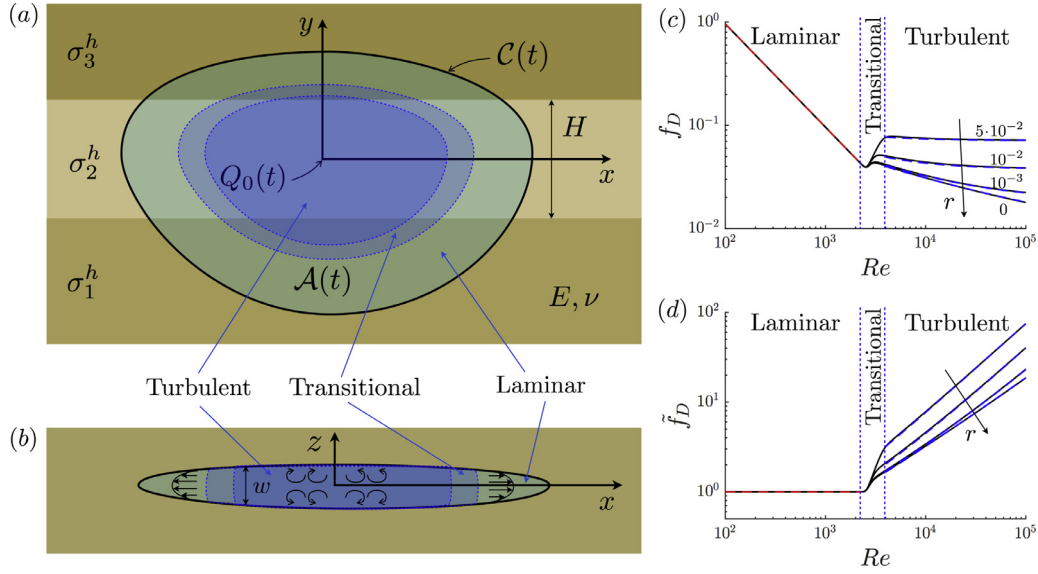


Fig. 1. (a) Schematics of a planar fracture with a footprint $A(t)$ inscribed within the curve $C(t)$. The point source with intensity $Q_0(t)$ is located at the origin of the (x, y) coordinate system and the far-field compressive stress varies from one layer to another. Zones of laminar, transitional, and fully turbulent fluid flow inside the fracture are shown schematically. (b) The variation of the fracture width along the x direction. Zones of laminar, transitional, and fully turbulent fluid flows inside the fracture are schematically shown. (c) Variation of the friction factor versus Reynolds number and relative roughness calculated using (5). The laminar friction factor is shown by the dashed red line and the fully turbulent friction factor, that is calculated using the Colebrook equation (Colebrook, 1939), is shown by the dashed blue lines. (d) Variation of the viscosity multiplier versus Reynolds number and relative roughness calculated using (7). (For interpretation of the references to color in this figure legend, the reader is referred to the web version of this article.)

$$A = \left(2.457 f_0 \left(Re, \frac{\epsilon}{D}\right)\right)^{16}, \quad B = \left(\frac{37530}{Re}\right)^{16},$$

$$f_0(Re, r) = \left| \log \left(\left(\frac{7}{Re} \right)^{0.9} + 0.27r \right) \right|. \quad (6)$$

The hydraulic diameter for non-circular pipes is defined as $D = 4A/P$, where A is the cross-sectional area of the pipe and P is the perimeter of the pipe. It is equal to $D = 2w$ for hydraulic fractures since the fluid flow in a fracture is locally equivalent to the flow between two parallel plates. For the purpose of hydraulic fracture modeling, it is convenient to factor the “laminar” term in Eq. (5) as

$$f_D = \frac{96}{Re} \tilde{f}_D, \quad \tilde{f}_D(Re, r) = \left(1 + (\tilde{A} + \tilde{B})^{-1.5}\right)^{1/12}, \quad (7)$$

where the new parameters are

$$\tilde{A} = \left[\frac{8.511}{Re^{1/2}} f_0(Re, r) \right]^{16}, \quad \tilde{B} = \left(\frac{2566}{Re} \right)^{24}, \quad Re = \frac{24\rho U w}{\mu'},$$

$$r = \frac{\epsilon}{2w}. \quad (8)$$

By substituting (7) into (4), one finds the expression for the flux in the form

$$\mathbf{q} = \mathbf{U} w = - \frac{w^3}{\mu' \tilde{f}_D(Re, r)} \nabla p. \quad (9)$$

The above expression for the fluid flux resembles the standard relation for laminar flow that is commonly used in hydraulic fracturing simulators, but features an additional multiplier $\tilde{f}_D(Re, r)$. This multiplier has the meaning of an apparent viscosity factor, in the sense that the pressure drop for the turbulent flow is equivalent to the pressure drop of a laminar flow with the viscosity multiplied by the factor $\tilde{f}_D(Re, r)$. In addition, the Reynolds number depends on the absolute value of the average velocity $U = \sqrt{U_x^2 + U_y^2}$, where $\mathbf{U} = (U_x, U_y)$. In this situation, the x and y components of the flux are coupled. To illustrate the variation of the friction factor f_D and its apparent viscosity counterpart \tilde{f}_D , their dependence

on the Reynolds number is plotted in Fig. 1(c and d) for different values of relative roughness r . The laminar solution is indicated by the dashed red lines for $Re < 2300$ and the fully turbulent solution, which is calculated using the Colebrook equation for $Re > 4000$ (Colebrook, 1939) (the latter is used in the Moody chart), is shown by the dashed blue lines. Note that the study (Wang and Hou, 2014) provides a recent experimental validation of the Moody chart. As can be seen from the comparison on the Fig. 1(c and d), Churchill’s equation is able to accurately capture the laminar and fully turbulent flows and smoothly connects the data in the transitional zone. Regarding the magnitude of fracture roughness, it depends on the rock type. To provide a realistic estimate, one can utilize results of the study (Wu and Sharma, 2017), in which a fracture surface profile was measured by an optical profiler. The amplitude of the roughness is shown to be on the order of tens of micrometers. Given that the hydraulic fracture width is typically equal to a few millimeters, the relative roughness becomes $O(10^{-2})$, which indicates that if the turbulent flow develops in hydraulic fractures, it will likely correspond to the flow in rough channels, see Fig. 1(c).

To describe the fracture front evolution, the classical LEFM solution for the mode I crack tip (Rice, 1968) is employed, so that

$$\lim_{s \rightarrow 0} \frac{w}{s^{1/2}} = \frac{K'}{E'}, \quad \text{if } V > 0, \quad \lim_{s \rightarrow 0} \frac{w}{s^{1/2}} = \frac{K'_I}{E'}, \quad \text{if } V = 0, \quad (10)$$

where s is the distance from a point inside the fracture to the fracture front, V is the velocity of the fracture front, and K'_I is the stress intensity factor for a non-propagating fracture. However, it was shown that the validity region of the square root width solution (10) is often very small for fluid-filled cracks (Desroches et al., 1994; Lenoach, 1995; Detournay and Garagash, 2003; Garagash et al., 2011; Dontsov and Peirce, 2015b). Therefore, it is necessary to use a different solution to accurately capture the propagation of a hydraulic fracture. As a result, the fracture propagation in the numerical algorithm is prescribed through the relation

$$w(s) = w_a(s), \quad (11)$$

where $w_a(s)$ is the so-called tip asymptotic solution and s is the distance from a point inside the fracture to the fracture front. This solution is obtained by analyzing the problem of a semi-infinite hydraulic fracture, and was first obtained numerically in Garagash et al. (2011) for the case of a brittle fracture driven by a Newtonian fluid in a permeable formation (as considered in this study). Later, a closed form approximation for this problem (i.e. for w_a) was obtained in Dontsov and Peirce (2015b) and this approximate solution is used in this study due to its ability to provide rapid results. Note that the solution (11) is valid further away from the fracture tip than the LEFM solution (10) and automatically reduces to it for smaller distances to the fracture front. In addition to the propagation condition (11), one should also prescribe a zero flux condition (Detournay and Peirce, 2014) at the fracture front as

$$\lim_{s \rightarrow 0} w^3 \frac{\partial p}{\partial s} = 0, \quad (12)$$

which ensures that the crack and fluid fronts coincide since the model does not account for the effect of fluid lag (Garagash and Detournay, 2000). Note here that the fluid lag decreases significantly in size for large *in situ* stress and can be estimated to be on the order of millimeters for deep unconventional reservoirs. Since the typical element size is measured in meters, the effect of the fluid lag can be ignored in the computations.

An Implicit Level Set Algorithm (ILSA) (Peirce and Detournay, 2008; Peirce, 2015; Dontsov and Peirce, 2017) is used to obtain the numerical solution for the problem (2), (3), (7)–(9), (11), and (12). A similar problem for the case of laminar fluid flow was solved numerically recently using the ILSA scheme in Dontsov and Peirce (2017). Since the primary difference in the numerical algorithm used for the current problem is the presence of the viscosity multiplier \tilde{f}_D in (9), which does not require noticeable changes to the algorithm, readers are referred to Dontsov and Peirce (2017) for details of the numerical implementation of the ILSA scheme. A different numerical algorithm is used for the case of an axisymmetric hydraulic fracture. It utilizes the radial symmetry and a moving mesh to provide a computationally efficient numerical solution. Such an algorithm for a radial hydraulic fracture driven by laminar fluid flow can be found in Dontsov (2016a) and is therefore is not included into this paper. The ILSA scheme yields similar results for the axisymmetric problem, which are not presented here.

3. Laminar-to-turbulent transition for an axisymmetric hydraulic fracture

Firstly, we consider the case of an axisymmetric hydraulic fracture. This situation occurs when the fracture diameter is less than the height of the primary layer, H , see Fig. 1(a), or when $\sigma_1^h = \sigma_2^h = \sigma_3^h$. To cater for slick water hydraulic fracture treatments, the following material parameters are chosen for the calculations

$$\begin{aligned} E' &= 9.9 \times 10^9 \text{ Pa}, & \mu' &= 1.2 \times 10^{-2} \text{ Pa}\cdot\text{s}, \\ K' &= 1.6 \times 10^6 \text{ MPa}\cdot\text{m}^{1/2}, & C' &= 0 \text{ m/s}^{1/2}, \\ Q_0 &= 0.2 \text{ m}^3/\text{s}, & \epsilon &= \{10^{-4}, 10^{-5}, 10^{-6}\} \text{ m}, \\ \rho &= 1000 \text{ kg/m}^3. \end{aligned} \quad (13)$$

The time interval for calculations is selected as $0.1 < t < 10^3$ s. For the case of no turbulence and no leak-off, the fracture can propagate in the viscosity dominated, in the toughness dominated regime, or be in the transitional region between the two (Dontsov, 2016a; Madyarova, 2003). The time scale that characterizes this transition is

$$t_{mk} = \left(\frac{\mu'^5 E'^{13} Q_0^3}{K'^{18}} \right)^{1/2},$$

which for the parameters (13), is equal to $t_{mk} \approx 2 \times 10^3$ s. The corresponding dimensionless time $\tau = t/t_{mk}$ is in the

range of $5 \times 10^{-5} < \tau < 0.5$. The transition between the viscosity dominated and the toughness dominated regimes occurs for $0.045 \lesssim \tau \lesssim 2.6 \times 10^6$ (Dontsov, 2016a), while the fracture propagates in the viscosity regime for smaller times and in the toughness regime for larger times. The range of the dimensionless time for the considered problem parameters indicates that the hydraulic fracture propagates almost entirely within the viscosity dominated (or M) regime. At larger times, it starts to transition towards the toughness dominated solution. Note that the above propagation regimes ignore the effects of turbulence. However, since the turbulence effectively increases the viscosity, it is expected that the overall dominance of the viscosity over toughness can only increase. Also, this analysis demonstrates that once the turbulent effects diminish, the solution should correspond to the laminar viscosity dominated solution.

Results of the numerical calculations for the axisymmetric hydraulic fracture for the parameters (13) are shown in Fig. 2. Note that three different values of surface roughness are considered. The solid black lines indicate the numerical solution for the case when the turbulent fluid flow is considered (i.e. the flow can be either turbulent, laminar, or to be in transition). The dashed blue lines correspond to the numerical solution that assumes laminar fluid flow throughout the fracture. Note that the numerical solution is used for the laminar case since the laminar solution is at the onset of the transition from the viscosity dominated to the toughness dominated regime of propagation and the use of the limiting viscosity-dominated M solution may cause some discrepancies. The approximate solution for the radial hydraulic fracture (Dontsov, 2016a) could have been used as well. Also note that the same discretization is used for the laminar and turbulent numerical solutions. Fig. 2(a) shows the variation of the fracture radius that is normalized by the laminar solution versus time, Fig. 2(b) shows the variation of the fracture width at the wellbore (also normalized by the laminar solution) versus time, Fig. 2(c) shows the spatial variation of the fracture aperture for $t = \{1, 10, 100\}$ s, and Fig. 2(d) shows the spatial variation of the fluid pressure at $t = 100$ s. Only one time instant for the pressure plot is selected since the addition of other pressure solutions leads to multiple overlapping, which reduces legibility of the figure. As can be seen from Fig. 2(a and b), there is a transition with time from the turbulence dominated solution to the laminar viscosity dominated solution. In addition, the transition region increases for smaller values of roughness. It should be noted here that the turbulence dominated solution is actually a viscosity-turbulent solution, which is different from the leak-off-turbulent solution that occurs for large values of leak-off, as shown in Dontsov (2016b) for the case of a semi-infinite hydraulic fracture.

One peculiar feature of the solution is that the fracture width at the wellbore does not change with time for the turbulent regime, even though the fracture grows in the radial direction, as can be seen from Fig. 2(c). The near wellbore behavior is dominated by turbulence due to the large fluid velocities near the concentrated source. In particular, the fracture becomes locally wider and there is a much more significant pressure drop near the wellbore, see Fig. 2(d). For the point source, as considered in this study, the fluid pressure has a singularity at the origin. The fluid flux is $q \propto 1/r$ near the origin, the pressure gradient for the laminar case is $\partial p / \partial r \propto q$, while for the turbulent case it can be shown that $\partial p / \partial r \propto q^2$. So that the pressure has a logarithmic singularity $p \propto \log r$ for the laminar case and a much stronger singularity $p \propto 1/r$ for the turbulent case. Note that the strong pressure drop near the wellbore occurs even when the fracture radius is nearly equal to the corresponding radius for the laminar solution (see the $t = 100$ s case). This indicates that the turbulent fluid flow may affect the near wellbore

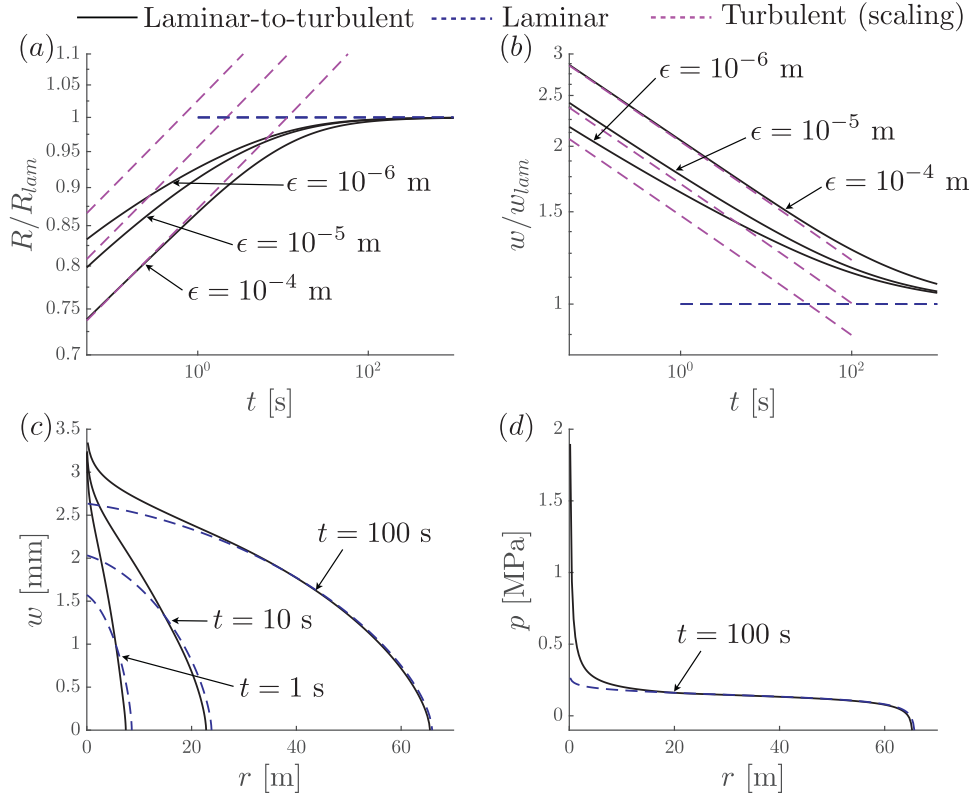


Fig. 2. The solid black lines indicate the numerical solution for the case when turbulent flow within the axisymmetric hydraulic fracture is possible. The dashed blue lines indicate the numerical solution for the case when solely laminar fluid flow is considered. The dashed magenta lines indicate the turbulence dominated solution that is obtained using scaling considerations, see (15). (a) Hydraulic fracture radius (normalized by the laminar solution) versus time. (b) Hydraulic fracture aperture at the source (normalized by the laminar solution) versus time. (c) Spatial variation of the fracture width at different time instants $t = \{1, 10, 100\}$ s for $\epsilon = 10^{-4}$ m. (d) Spatial variation of the fluid pressure at $t = 100$ s for $\epsilon = 10^{-4}$ m. (For interpretation of the references to color in this figure legend, the reader is referred to the web version of this article.)

features even in situations when the fracture's global behavior follows the laminar solution.

To better understand the behavior of a radial hydraulic fracture driven by turbulent fluid flow, and, in particular, to quantify why the fracture width does not change with time (see Fig. 2(c)), it is necessary to consider the fracture behavior in the limit when the fully developed turbulent flow occurs within the most of the fracture. Rigorous analysis of the multiscale hydraulic fracture behavior (as was done in Dontsov, 2016a; Madyarova, 2003 for laminar flow) for the case of the turbulent flow is beyond the scope of this study. Instead, a qualitative explanation based on scaling will be given and only the transition from the turbulence dominated to the viscosity dominated regime will be considered. Firstly, the toughness can be neglected since the viscosity dominates for the laminar case and turbulence can only increase the apparent viscosity. In the absence of leak-off and toughness, the elasticity Eq. (2), the continuity Eq. (3), the flux Eq. (9), and the friction factor relation (7) (simplified for large Reynolds numbers, see Dontsov (2016b)) can be written as

$$p \sim E' \frac{w}{R}, \quad \frac{w}{t} \sim \frac{q}{R} \sim \frac{Q_0}{R^2}, \quad q \sim \frac{w^3}{\mu' \tilde{f}_D R}, \quad \tilde{f}_D \sim \frac{\rho q}{\mu' f_0^2}, \quad (14)$$

where the “ \sim ” symbol indicates the equivalence of scales. The f_0 , defined in (6), varies slowly with the parameters, in which case it is treated as a time-independent constant. The scaling relations in (14) allow us to obtain temporal variations for the fracture width, radius, and pressure as

$$w_t = C_w \left(\frac{Q_0}{f_0} \right)^{1/2} \left(\frac{\rho}{E'} \right)^{1/4}, \quad R_t = C_R (f_0 Q_0)^{1/4} \left(\frac{E'}{\rho} \right)^{1/8} t^{1/2}, \quad w_m = 1.19 \left(\frac{\mu'^2 Q_0^3 t}{E'^2} \right)^{1/9}, \quad R_m = 0.69 \left(\frac{Q_0^3 E' t^4}{\mu'} \right)^{1/9}. \quad (16)$$

$$p_t = C_p E' \left(\frac{Q_0}{f_0} \right)^{1/4} \left(\frac{\rho}{E'} \right)^{3/8} t^{-1/2}, \quad (15)$$

where the subscript “ t ” is added to indicate that the scaling is valid for the situation when turbulent flow dominates the response, and C_w , C_R , C_p are time independent constants. The above equation indicates that the fracture width magnitude does not change with time, which is consistent with the results shown in Fig. 2(c). To further illustrate the validity of (15), the dashed magenta lines in Fig. 2 show the temporal variations of the fracture width and radius calculated using (15). Note that the proportionality constants are $C_w = 0.94$ for the fracture width and $C_R = 0.98$ for the fracture radius in (15). Here the value of f_0 is calculated assuming that the Reynolds number is equal to infinity. It can be easily shown that the roughness primarily determines the value of f_0 for large Reynolds numbers. Since the fracture width is found to be independent of time for the turbulence dominated regime, there is no variation of the relative roughness and hence the function f_0 can indeed be treated as a time-independent constant. Note that the value of C_p depends on the spatial location inside the fracture at which the pressure is evaluated. Since the latter is singular at the wellbore, this location cannot be taken at the origin.

To estimate the transition time from the turbulence dominated to the viscosity dominated (laminar) solution, we need to consider solution for the radial hydraulic fracture solution propagating in the viscosity dominated regime, which can be summarized as follows (Dontsov, 2016a; Madyarova, 2003)

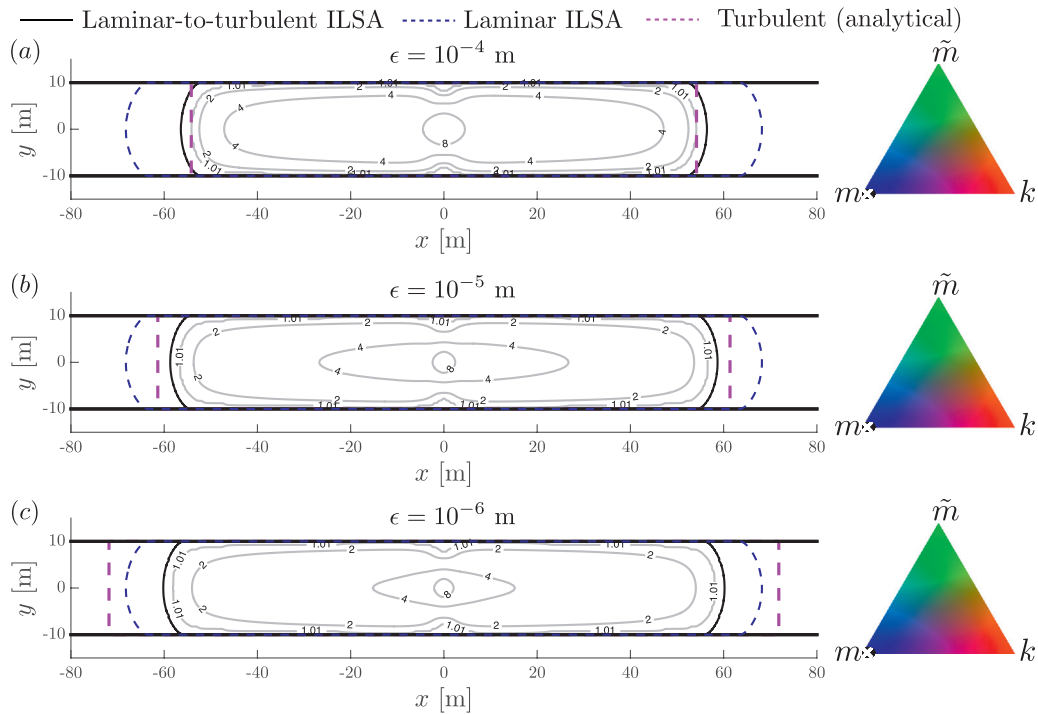


Fig. 3. Fracture footprints for the PKN fracture geometry for different values of surface roughness: (a) $\epsilon = 10^{-4}$ m, (b) $\epsilon = 10^{-5}$ m, (c) $\epsilon = 10^{-6}$ m. The black solid lines indicate the numerical ILSA solution that accounts for the laminar-to-turbulent fluid flow. The dashed blue lines indicate the ILSA solution, in which the fluid flow is forced to be laminar. The dashed magenta lines show the predictions of the analytical solution for a completely turbulent PKN fracture (20). The grey contour lines inside the fractures indicate constant values of the viscosity multiplier \tilde{f}_D (7). The parametric triangles indicate the tip asymptotic solutions that are used to advance the fracture front. The black circular markers inside the triangles correspond to the turbulent ILSA solution and the white crosses represent the laminar ILSA solution. (For interpretation of the references to color in this figure legend, the reader is referred to the web version of this article.)

By considering either $w_m = w_t$ or $R_m = R_t$ the characteristic time scale for the transition can be obtained using (15) and (16) as

$$t_{tm} = C_{tm} \frac{\rho^{9/4} Q_0^{3/2}}{f_0^{9/2} \mu^2 E^{1/4}}. \quad (17)$$

The proportionality constant C_{tm} in the above expression depends on whether $w_m = w_t$ or $R_m = R_t$ is used. For the $w_m = w_t$ case $C_{tm} = 0.12$. On the other hand, for the $R_m = R_t$ case $C_{tm} = 1.8 \times 10^{-3}$. As a result, the transition time for the fracture width case (in which it is assumed that $\epsilon = 10^{-4}$ m) is 630 s and for the fracture radius case is 9.5 s, which is consistent with the results shown in Fig. 2(a) and (b).

The transition time in (17) with the proportionality constant $C_{tm} = 1.8 \times 10^{-3}$ can be used to estimate whether the laminar or turbulent solution should be used to estimate the hydraulic fracture radius. In particular, if the treatment time t is such that $t \ll t_{tm}$, then the turbulent solution applies, however, if $t \gg t_{tm}$ then the laminar solution should be used. Note that the above conclusion applies only for the fracture radius estimation and for the transition from the turbulence dominated to the viscosity dominated regime, i.e. assuming no leak-off and negligible fracture toughness. Similar analyses can be performed for the other cases to quantify the effect of toughness, leak-off, and the associated transitions.

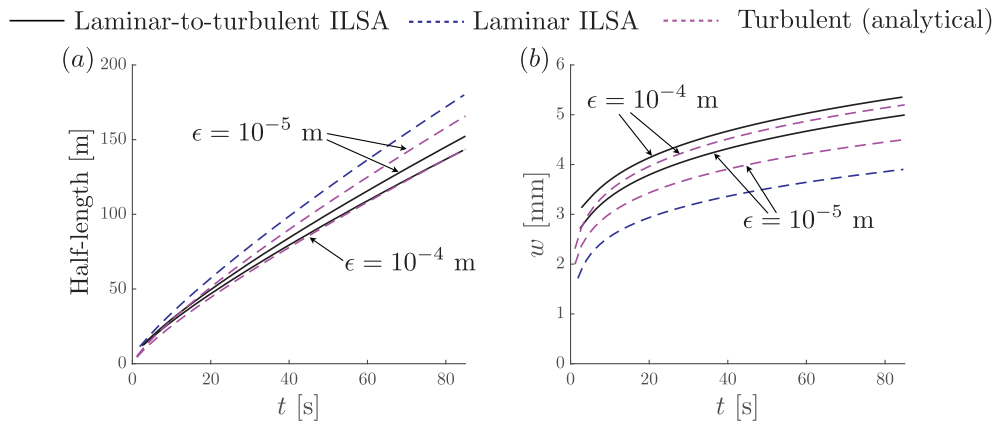


Fig. 4. Time histories of the fracture half-length (a) and wellbore width (b) for PKN fracture geometry for different values of surface roughness. The black solid lines indicate the numerical ILSA solution that accounts for the laminar-to-turbulent fluid flow. The dashed blue lines indicate the ILSA solution, in which the fluid flow is forced to be laminar. The dashed magenta lines show the predictions of the analytical solution for a completely turbulent PKN fracture (20). (For interpretation of the references to color in this figure legend, the reader is referred to the web version of this article.)

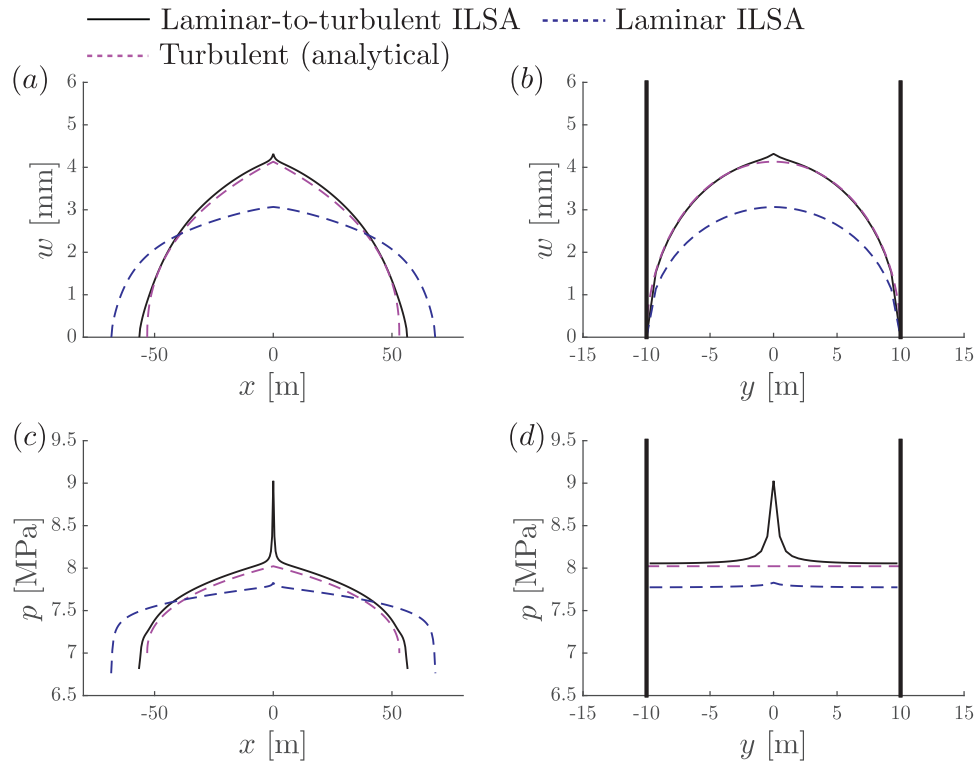


Fig. 5. Variation of the fracture width along the x axis (a) and the y axis (b) and variation of the fluid pressure along the x axis (c) and the y axis (d) for PKN fracture geometry for $\epsilon = 10^{-4}$ m. The black solid lines indicate the numerical ILSA solution that accounts for the laminar-to-turbulent fluid flow. The dashed blue lines indicate the ILSA solution, in which the fluid flow is forced to be laminar. The dashed magenta lines show the predictions of the analytical solution for a completely turbulent PKN fracture (20). (For interpretation of the references to color in this figure legend, the reader is referred to the web version of this article.)

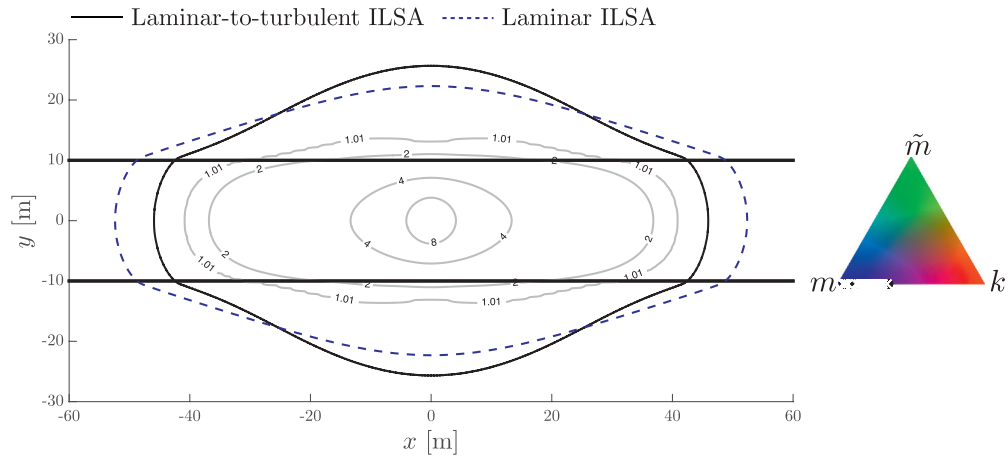


Fig. 6. Fracture footprints for the fracture geometry with symmetric stress barriers. The black solid lines indicate the numerical ILSA solution that accounts for the laminar-to-turbulent fluid flow. The dashed blue lines indicate the ILSA solution, in which the fluid flow is forced to be laminar. The grey contour lines inside the fractures indicate the constant values of the viscosity multiplier \tilde{f}_b (7). The parametric triangle indicates the tip asymptotic solutions that are used to advance the fracture front. The black circular markers correspond to the turbulent ILSA solution and the white crosses represent the laminar ILSA solution. (For interpretation of the references to color in this figure legend, the reader is referred to the web version of this article.)

4. Numerical solution for the three stress layers geometry using an Implicit Level Set Algorithm (ILSA)

This section presents the numerical results obtained using the hydraulic fracturing simulator ILSA for the planar fracture propagating in the three stress layer system shown in Fig. 1(a). The default parameters that are used in all simulations are

$$\begin{aligned}
 E' &= 9.9 \times 10^9 \text{ Pa}, & \mu' &= 1.2 \times 10^{-2} \text{ Pa} \cdot \text{s}, \\
 K' &= 1.6 \times 10^6 \text{ MPa} \cdot \text{m}^{1/2}, & C' &= 0 \text{ m/s}^{1/2}, \\
 Q_0 &= 0.2 \text{ m}^3/\text{s}, & \epsilon &= 10^{-4} \text{ m}, & \rho &= 1000 \text{ kg/m}^3,
 \end{aligned}$$

$$H = 20 \text{ m}, \tag{18}$$

unless otherwise stated.

Figs. 3–5 present the results for the PKN fracture geometry, for which

$$\sigma_2^h = 7 \text{ MPa}, \tag{19}$$

and the fracture propagation is restricted to the central layer, which is equivalent to having very large values for σ_1^h and σ_3^h . Fig. 3 plots the fracture footprints at $t = 25$ s for different values of surface roughness. The numerical ILSA solution is compared to

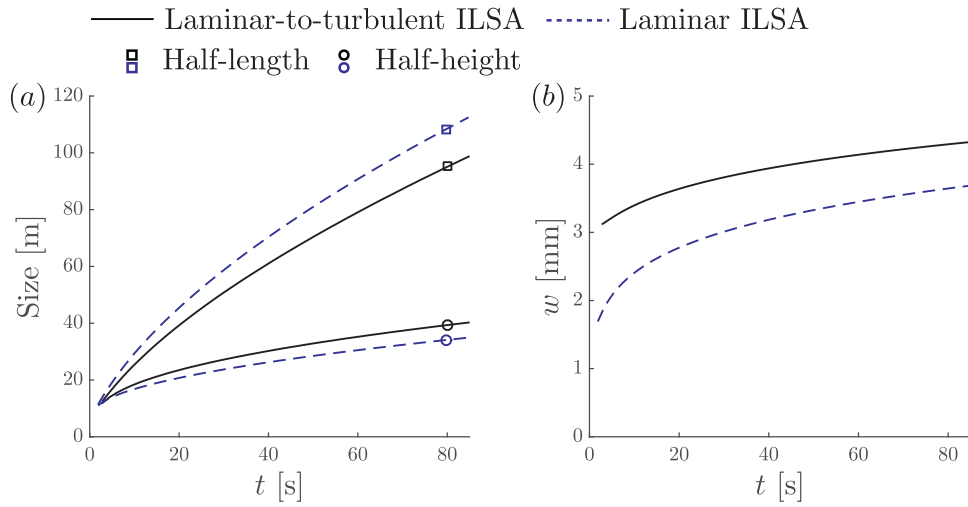


Fig. 7. Time histories of the fracture half-length and half-height (a) and wellbore width (b) for the fracture geometry with symmetric stress barriers. The black solid lines indicate the numerical ILSA solution that accounts for the laminar-to-turbulent fluid flow. The dashed blue lines indicate the ILSA solution, in which the fluid flow is forced to be laminar. (For interpretation of the references to color in this figure legend, the reader is referred to the web version of this article.)

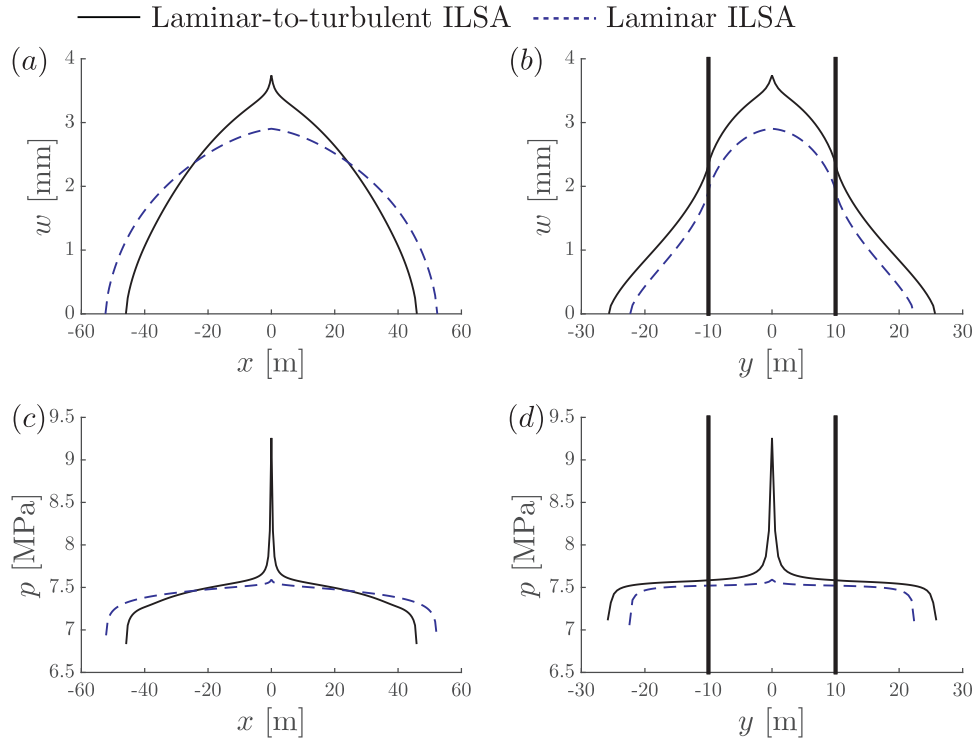


Fig. 8. Variation of the fracture width along the x axis (a) and the y axis (b) and variation of the fluid pressure along the x axis (c) and the y axis (d) for the fracture geometry with symmetric stress barriers. The black solid lines indicate the numerical ILSA solution that accounts for the laminar-to-turbulent fluid flow. The dashed blue lines indicate the ILSA solution, in which the fluid flow is forced to be laminar. (For interpretation of the references to color in this figure legend, the reader is referred to the web version of this article.)

its analog that is forced to have laminar fluid flow and to the analytical solution developed in Zolfaghari et al. (2017b) that assumes a fully turbulent flow in a rough channel. The latter can be summarized as

$$l(t) = 2.1619 \frac{Q_0}{H} \left(\frac{H^2 E'}{2 \epsilon^{1/3} Q_0^3 \rho} \right)^{3/16} t^{13/16},$$

$$w(x, t) = 0.8122 \left(\frac{2 \epsilon^{1/3} Q_0^3 \rho}{H^2 E'} \right)^{3/16} t^{3/16} (1 - \xi)^{3/7} (1 + 0.05497 \xi),$$

$$\xi = \frac{x}{l(t)}.$$

$$p(x, t) = 0.8122 \left(\frac{\epsilon Q_0^9 \rho^3 E'^{13}}{2^{13} H^{22}} \right)^{1/16} t^{3/16} (1 - \xi)^{3/7} (1 + 0.05497 \xi). \quad (20)$$

The parametric triangle indicates the asymptotic solutions that are used to advance the fracture front in the ILSA scheme, see Dontsov and Peirce (2017) for details. The black circular markers inside the triangle correspond to the turbulent ILSA solution and the white crosses are related to the laminar ILSA solution. The results indicate that the viscosity-dominated tip asymptote (the m vertex) is used in all calculations. The grey contour lines inside the fracture footprint indicate constant values of \tilde{f}_D (7), which is a parameter that reflects the apparent fluid viscosity multiplier.

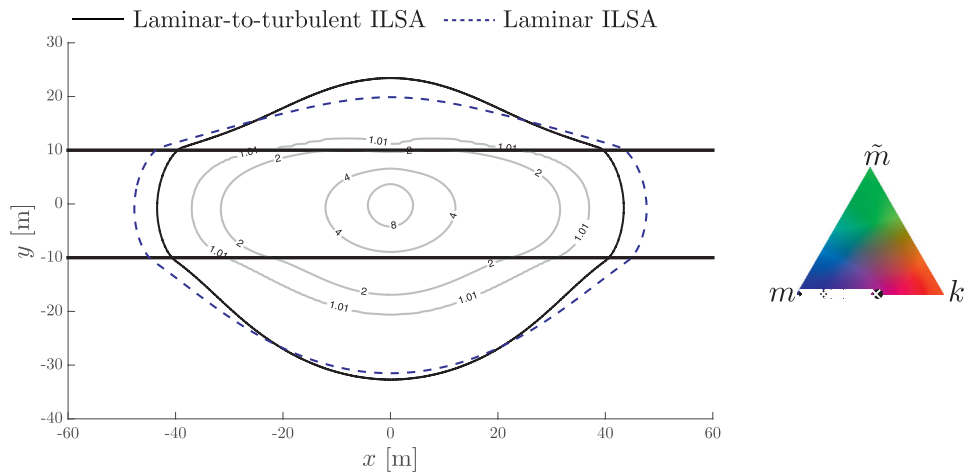


Fig. 9. Fracture footprints for the fracture geometry with asymmetric stress barriers. The black solid lines indicate the numerical ILSA solution that accounts for the laminar-to-turbulent fluid flow. The dashed blue lines indicate the ILSA solution, in which the fluid flow is forced to be laminar. The grey contour lines inside the fractures indicate the constant values of the viscosity multiplier \tilde{f}_D (7). The parametric triangle indicates the tip asymptotic solutions that are used to advance the fracture front. The black circular markers correspond to the turbulent ILSA solution and the white crosses represent the laminar ILSA solution. (For interpretation of the references to color in this figure legend, the reader is referred to the web version of this article.)

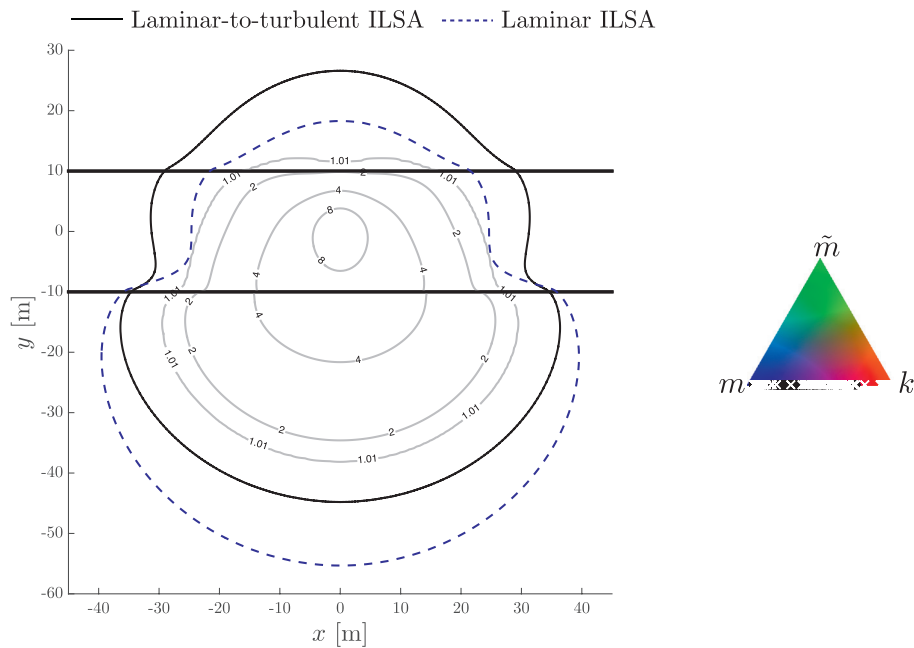


Fig. 10. Fracture footprints for the fracture geometry with stress drop configuration. The black solid lines indicate the numerical ILSA solution that accounts for the laminar-to-turbulent fluid flow. The dashed blue lines indicate the ILSA solution, in which the fluid flow is forced to be laminar. The grey contour lines inside the fractures indicate the constant values of the viscosity multiplier \tilde{f}_D (7). The parametric triangle indicates the tip asymptotic solutions that are used to advance the fracture front. The black circular markers correspond to the turbulent ILSA solution and the white crosses represent the laminar ILSA solution. (For interpretation of the references to color in this figure legend, the reader is referred to the web version of this article.)

The results in Fig. 3 indicate that the turbulence makes the fracture shorter and that the approximate PKN solution (20) is able to accurately estimate the fracture length only for the largest considered value of surface roughness $\epsilon = 10^{-4}$ m. Smaller values of the surface roughness lead to inaccurate estimates of the fracture length. The analytical solution predicts a fracture that is longer than the laminar solution for $\epsilon = 10^{-6}$ m case, which is not consistent since the turbulence should always make the fracture shorter. Fig. 4 plots the time histories of the fracture length and wellbore width for the ILSA numerical solution (solid black lines), laminar ILSA solution (dashed blue lines), and the approximate turbulent PKN solution (dashed magenta lines). The results agree with the previous observation that the turbulence introduces additional vis-

cus resistance, which makes the fracture shorter as compared to the laminar solution, and that the approximate PKN solution is able to capture the turbulent behavior only for the large roughness case. The discrepancy between the numerical ILSA solution and the analytical solution (20) comes from the fact that the latter utilizes the Gauckler-Manning-Strickler (Manning, 1891; Strickler, 1981) friction factor that applies for a fully turbulent fluid flow in a rough channel. In particular, this model assumes a constant friction factor, which applies for large Reynolds numbers and relatively large values of roughness as shown by the flat horizontal curves in Fig. 1(c) for $0.01 \leq r \leq 0.05$). Consequently, it does not provide a good estimate for the cases with smaller roughness that are closer to the smooth channel case. In addition, the values of

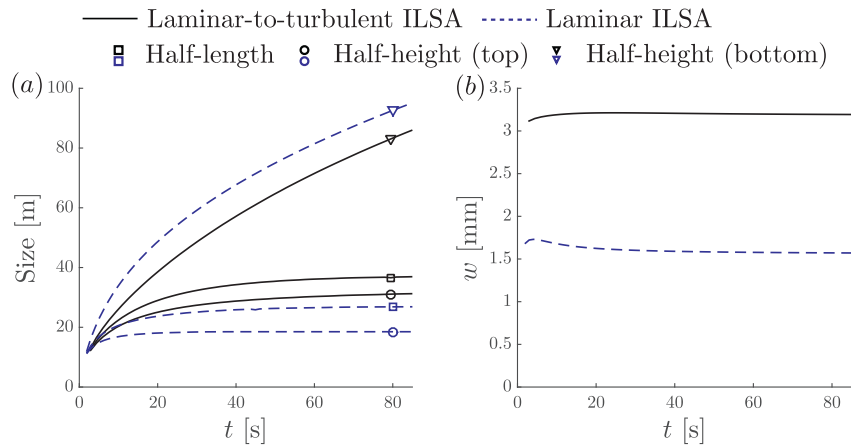


Fig. 11. Time histories of the fracture half-length and half-height (a) and wellbore width (b) for the fracture geometry with stress drop configuration. The black solid lines indicate the numerical ILSA solution that accounts for the laminar-to-turbulent fluid flow. The dashed blue lines indicate the ILSA solution, in which the fluid flow is forced to be laminar. (For interpretation of the references to color in this figure legend, the reader is referred to the web version of this article.)

the effective viscosity multiplier (shown by the grey solid lines) are smaller for the $\epsilon = 10^{-5}$ m and $\epsilon = 10^{-6}$ m cases. This shows that the effect of turbulent flow is less pronounced for these values of roughness, which may also be the reason for the disagreement between the numerical and the analytical solutions. Fig. 5 plots the fracture width and pressure along the x and y axes at $t = 25$ s for $\epsilon = 10^{-4}$ m. Comparison between the numerical ILSA solution and the laminar solution indicates that the fracture is shorter and wider if turbulence is considered. In addition, there is a strong pressure spike and a less pronounced width spike in the vicinity of the wellbore, which is caused by the turbulent flow. This behavior is similar to that for a radial fracture, see Fig. 2. The analytical solution (20) is able to accurately estimate the fracture width and pressure variations, but does not account for the pressure spike near the wellbore. Note that the characteristic fracture width is equal to a few millimeters, in which case the normalized roughness $\epsilon/(2w) = O(10^{-2})$ for $\epsilon = 10^{-4}$ m. This value of the normalized roughness corresponds to the “flat” behavior of the friction factor for large Reynolds numbers (see Fig. 1(c)), so that the analytic model (20) gives good results in this case. However, if the roughness is reduced to $\epsilon = 10^{-5}$ m or less, then $\epsilon/(2w) = O(10^{-3})$ or less and the constant Gauckler-Manning-Strickler friction factor no longer applies, in which case (20) underestimates the effective viscosity.

To investigate the effect of turbulent fluid flow on the hydraulic fracture geometry for more complex cases, Figs. 6–13 present the results for various layered stress configurations. There are three main cases: symmetric stress barrier, asymmetric stress barrier, and stress drop. They represent typical situations, in which there are only three layers present in the formation. In addition, to study the effect of fluid leak-off, an additional stress drop case is considered. These solutions provide useful physical insights of the effect of turbulent flow for various cases and can also be used as reference solutions to evaluate accuracy of the reduced models, such as pseudo-3D models, see e.g. Dontsov and Peirce (2015a) for the case of the laminar fluid flow.

Figs. 6–8 present the results for the symmetric stress barrier case, for which the compressive stresses are prescribed as

$$\sigma_1^h = \sigma_3^h = 7.5 \text{ MPa}, \quad \sigma_2^h = 7 \text{ MPa}. \quad (21)$$

Fig. 6 plots the fracture footprints at $t = 25$ s. The numerical ILSA solution is compared to the numerical ILSA solution that is forced to have laminar fluid flow. Fig. 7 presents the results for the fracture half-length, the half-height, and the wellbore width versus time. Fig. 8 shows the fracture width and pressure along the x and

y axes at $t = 25$ s. These results demonstrate that the additional resistance that is associated with the turbulent flow tends to produce a fracture with a more circular shape, which is not surprising since the turbulence effectively increases the fluid viscosity, which in turn causes a more circular fracture shape. By “more circular” we mean that the fracture length is smaller than that for the laminar solution and the fracture height is larger. In addition, the fracture is noticeably wider at the wellbore, as is clearly indicated in Fig. 7(b). The pressure and width peaks near the wellbore, which are associated with turbulent flow, are also present.

Fig. 9 shows the fracture footprint results for the asymmetric stress barrier fracture geometry, for which the compressive stresses are taken as

$$\sigma_1^h = 7.25 \text{ MPa}, \quad \sigma_2^h = 7 \text{ MPa}, \quad \sigma_3^h = 7.5 \text{ MPa}. \quad (22)$$

The results also indicate that the fracture tends to be more circular due to the turbulent flow. One interesting observation is that the fracture height growth through the higher stress barrier is more substantial in the laminar-to-turbulent ILSA solution compared to the laminar solution. Therefore, turbulent flow may facilitate crossing a high stress layer.

Figs. 10–12 present the results for the stress drop case, for which the compressive stresses are taken as

$$\sigma_1^h = 6.5 \text{ MPa}, \quad \sigma_2^h = 7 \text{ MPa}, \quad \sigma_3^h = 7.25 \text{ MPa}. \quad (23)$$

Figs. 10–12 plot similar quantities as Figs. 6–8. As for the asymmetric stress barrier case, the turbulent fluid flow promotes the fracture growth through the larger stress zone and reduces growth through the lower stress zone. In this case, the fracture footprint is effectively shifted upwards due to the turbulent flow. Fig. 11 plots time histories of the fracture dimensions as well as the wellbore width. As can be seen from the figure, the fracture dimensions appear to be closer to each other if the turbulence is considered, which also indicates that the fracture tends to be more circular in which case all the dimensions coincide. In addition, the fracture is nearly twice as wide at the wellbore compared to the predictions of the laminar solution. Fig. 12 provides a more detailed explanation by showing the fracture width and pressure profiles. In particular, it clearly demonstrates that the fracture width centroid is shifted upwards, which causes a substantial increase in the wellbore width.

Since the stress drop case demonstrated the strongest influence of the turbulent flow, Fig. 13 shows the additional effect of fluid leak-off on the solution for the same stress drop geometry. In par-

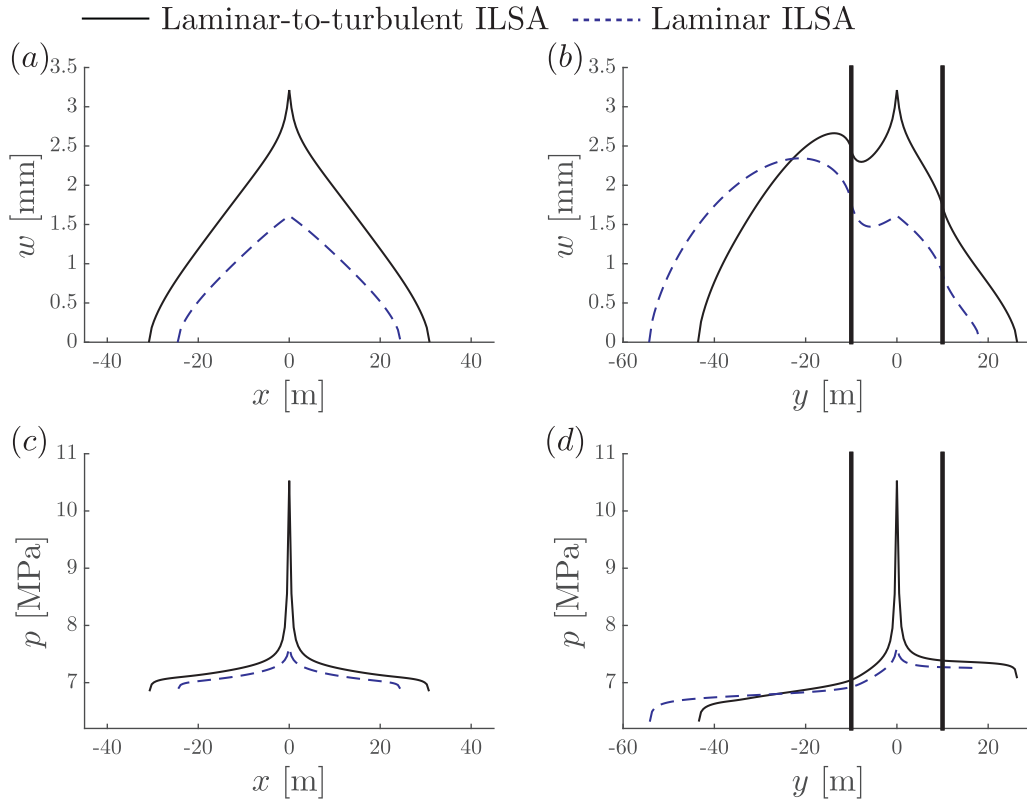


Fig. 12. Variation of the fracture width along the x axis (a) and the y axis (b) and variation of the fluid pressure along the x axis (c) and the y axis (d) for the fracture geometry with stress drop configuration. The black solid lines indicate the numerical ILSA solution that accounts for the laminar-to-turbulent fluid flow. The dashed blue lines indicate the ILSA solution, in which the fluid flow is forced to be laminar. (For interpretation of the references to color in this figure legend, the reader is referred to the web version of this article.)

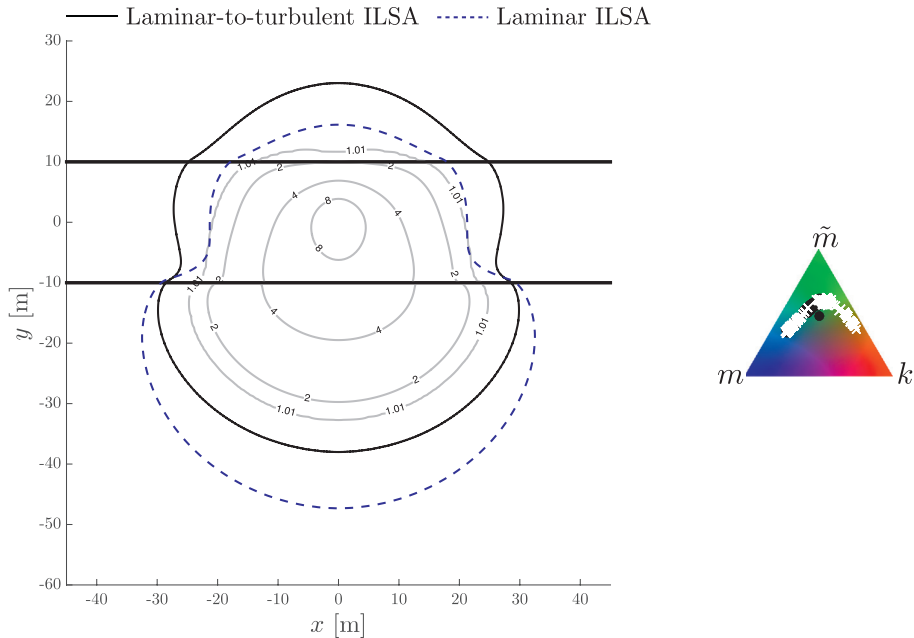


Fig. 13. Fracture footprints for the fracture geometry with stress drop configuration with leak-off. The black solid lines indicate the numerical ILSA solution that accounts for the laminar-to-turbulent fluid flow. The dashed blue lines indicate the ILSA solution, in which the fluid flow is forced to be laminar. The grey contour lines inside the fractures indicate the constant values of the viscosity multiplier \tilde{f}_D (7). The parametric triangle indicates the tip asymptotic solutions that are used to advance the fracture front. The black circular markers correspond to the turbulent ILSA solution and the white crosses represent the laminar ILSA solution. (For interpretation of the references to color in this figure legend, the reader is referred to the web version of this article.)

ticular, the value of the leak-off coefficient is taken as

$$C' = 6.9 \times 10^{-5} \text{ m/s}^{1/2},$$

which makes the fracture efficiency (ratio between the fracture volume and the total injected volume) approximately 70% at $t = 25$ s. Apart from having an overall smaller fracture and using different tip asymptotic solutions, the results appear to be similar to those shown in Fig. 10 for the no leak-off case.

To summarize, the results presented for the three stress layers geometry demonstrate that hydraulic fractures driven by turbulent fluid flow tend to be more circular and wider. In addition, the turbulent fluid flow promotes fracture growth into higher stress layers, which for the stress drop case shifts the whole fracture footprint significantly. Finally, fluid leak-off did not provide an additional substantial influence on the hydraulic fracture, apart from making the whole fracture smaller.

5. Summary

This study investigates the effect of turbulent fluid flow on planar hydraulic fractures. A friction factor that is able to capture the laminar, the turbulent, and the transitional fluid flow within the fracture is incorporated since the flow is always laminar in the vicinity of the fracture tip and can become turbulent further away from the tip. It is shown that from the hydraulic fracturing point of view, the turbulent flow effectively increases the fluid viscosity. The level of increase depends on the local Reynolds number and the relative surface roughness, which in turn depend on the local fluid velocity and the fracture width. As a result, the effective fluid viscosity variation is not uniform within the fracture. The effect is the most pronounced near the injection point and causes a strong pressure drop near the wellbore and a local fracture width increase.

Results are presented for different fracture geometries. Firstly, an axisymmetric or radial fracture is considered. It is shown that the solution can transition from the turbulence dominated solution to the viscosity dominated solution with time and the characteristic time scale for this transition is obtained. Time dependence of the fracture radius, width, and pressure for the turbulence dominated regime are obtained based on scaling considerations. An Implicit Level Set Algorithm (ILSA) is used to construct the solution for a three stress layer geometry. For the simplest PKN case, in which the fracture is contained within a single layer, the results are compared to the laminar solution and to the analytical solution that assumes turbulent fluid flow throughout the fracture. It is shown that the turbulence leads to a shorter fracture, which is consistent with the fact that the turbulence effectively increases the fluid viscosity. Also, the analytical solution is able to accurately estimate the fracture length when the fluid flow is fully turbulent and the fracture surface is rough. Results for the three stress layer cases indicate that the turbulent flow tends to produce a fracture that is more circular and to enhance the fracture growth through high stress zones. In addition, for the stress drop case, the whole fracture is effectively shifted by the turbulence towards the higher stress region. Finally, the addition of fluid leak-off did not add qualitatively new effects associated with turbulence.

Acknowledgements

AP acknowledges the support of the British Columbia Oil and Gas Commission and the NSERC discovery grants program. ED acknowledges start-up funds provided by the University of Houston.

References

Adachi, J., Siebrits, E., Peirce, A., Desroches, J., 2007. Computer simulation of hydraulic fractures. *Int. J. Rock Mech. Min. Sci.* 44, 739–757.

- Ames, B., Bunger, A., 2015. Role of turbulent flow in generating short hydraulic fractures with high net pressure in slickwater treatments. In: *Proceedings SPE Hydraulic Fracturing Technology Conference, Texas, USA, SPE 173373*.
- Anthonyrajah, M., Mason, D., Fareo, A., 2013. Propagation of a pre-existing turbulent fluid fracture. *Int. J. Nonlinear Mech.* 54, 105–114.
- Churchill, S., 1977. Friction factor equation spans all fluid flow regimes. *Chem. Eng.* 7, 91–92.
- Colebrook, C., 1939. Turbulent flow in pipes, with particular reference to the transition region between the smooth and rough pipe laws. *J. ICE* 11, 133–156.
- Crouch, S., Starfield, A., 1983. *Boundary Element Methods in Solid Mechanics*. George Allen and Unwin, London.
- Desroches, J., Detournay, E., Lenoach, B., Papanastasiou, P., Pearson, J., Thiercelin, M., Cheng, A.-D., 1994. The crack tip region in hydraulic fracturing. *Proc. R. Soc. Lond. A* 447, 39–48.
- Detournay, E., Garagash, D., 2003. The tip region of a fluid-driven fracture in a permeable elastic solid. *J. Fluid Mech.* 494, 1–32.
- Detournay, E., Peirce, A., 2014. On the moving boundary conditions for a hydraulic fracture. *Int. J. Eng. Sci.* 84, 147–155.
- Dontsov, E., 2016. An approximate solution for a penny-shaped hydraulic fracture that accounts for fracture toughness, fluid viscosity, and leak-off. *R. Soc. open sci.* 3, 160737.
- Dontsov, E., 2016. Tip region of a hydraulic fracture driven by a laminar-to-turbulent fluid flow. *J. Fluid. Mech.* 797, R2.
- Dontsov, E., Peirce, A., 2015. An enhanced pseudo-3D model for hydraulic fracturing accounting for viscous height growth, non-local elasticity, and lateral toughness. *Eng. Frac. Mech.* 142, 116–139.
- Dontsov, E., Peirce, A., 2015. A non-singular integral equation formulation to analyze multiscale behaviour in semi-infinite hydraulic fractures. *J. Fluid. Mech.* 781, R1.
- Dontsov, E., Peirce, A., 2017. A multiscale implicit level set algorithm (ILSA) to model hydraulic fracture propagation incorporating combined viscous, toughness, and leak-off asymptotics. *Comput. Methods Appl. Mech. Engrg.* 313, 53–84.
- Economides, M., Nolte, K., (Eds.), 2000. *Reservoir Stimulation*, 3rd. John Wiley & Sons, Chichester, UK.
- Garagash, D., Detournay, E., 2000. The tip region of a fluid-driven fracture in an elastic medium. *J. Appl. Mech.* 67, 183–192.
- Garagash, D., Detournay, E., Adachi, J., 2011. Multiscale tip asymptotics in hydraulic fracture with leak-off. *J. Fluid Mech.* 669, 260–297.
- Hills, D., Kelly, P., Dai, D., Korsunsky, A., 1996. *Solution of Crack Problems, The Distributed Dislocation Technique, Solid Mechanics and its Applications*, 44. Kluwer Academic Publisher, Dordrecht.
- Kano, M., Zolfaghari, N., Ames, B., Bunger, A., 2015. Solution for a pkn hydraulic fracture driven by turbulent fluid with large leak-off. *Hydraul. Fract. J.* 2, 34–38.
- Lenoach, B., 1995. The crack tip solution for hydraulic fracturing in a permeable solid. *J. Mech. Phys. Solids* 43, 1025–1043.
- Madyarova, M., 2003. *Fluid-Driven Penny-Shaped Fracture in Elastic Medium*. University of Minnesota Master's thesis.
- Manning, R., 1891. On the flow of water in open channels and pipes. *Trans. Inst. Civil Eng.* 20, 161–207.
- Moody, L.F., 1944. Friction factors for pipe flow. In: *Transactions of the ASME*, 66, pp. 671–684.
- Nilson, R., 1981. Gas-driven fracture propagation. *ASME J. Appl. Mech.* 48, 757–762.
- Nilson, R., F.A. Morrison, J., 1986. Transient gas or liquid flow along a pre-existing or hydraulically-induced fracture in a permeable medium. *ASME J. Appl. Mech.* 53, 157–165.
- Nordgren, R., 1972. Propagation of vertical hydraulic fractures. *Soc. Petrol. Eng. J.* 306–314.
- Peirce, A., 2015. Modeling multi-scale processes in hydraulic fracture propagation using the implicit level set algorithm. *Comp. Meth. in Appl. Mech. and Eng.* 283, 881–908.
- Peirce, A., Detournay, E., 2008. An implicit level set method for modeling hydraulically driven fractures. *Comput. Methods Appl. Mech. Engrg.* 197, 2858–2885.
- Perkins, T., Kern, L., 1961. Widths of hydraulic fractures. *J. Pet. Tech. Trans. AIME* 937–949.
- Rice, J., 1968. *Mathematical analysis in the mechanics of fracture*. In: Liebowitz, H. (Ed.), *Fracture: An Advanced Treatise*, vol. II. Academic Press, New York, NY, pp. 191–311. chapter 3
- Strickler, A., 1981. Contributions to the question of a velocity formula and roughness data for streams, channels and closed pipelines. Rep. T-10. Translated from German by T. Roegen et al., Lab. of Hydraul. and Water Resour., Calif. Inst. of Technol., Pasadena.
- Tsai, V., Rice, J., 2010. A model for turbulent hydraulic fracture and application to crack propagation at glacier beds. *J. Geophys. Res.* 115, F03007.
- Wang, Z., Hou, L., 2014. Experimental study on the friction coefficient of supercritical carbon dioxide in pipes. *Int. J. Greenh. Gas Control* 25, 151–161.
- Weng, X., 2015. Modeling of complex hydraulic fractures in naturally fractured formation. *J. Unconv. Oil and Gas Res.* 9, 114–135.
- Wu, W., Sharma, M., 2017. A model for the conductivity and compliance of unpropagated fractures. In: *SPE Hydraulic Fracturing Technology Conference and Exhibition*, 24:26 January, The Woodlands, Texas, USA, SPE-184852-MS. Society of Petroleum Engineers.
- Zolfaghari, N., Dontsov, E., Bunger, A., 2017a. Plane-strain model of a hydraulic fracture driven by turbulent fluid in an impermeable rock. *Int. J. Solids Struct.* Submitted to.
- Zolfaghari, N., Meyer, C., Bunger, A., 2017b. Blade-shaped (PKN) hydraulic fracture driven by a turbulent fluid in an impermeable rock. *arXiv:1609.01237*.